

Pre-perihelion evolution of the NiI/FeI abundance ratio in the coma of the interstellar comet 3I/ATLAS. From extreme to normal[★]

Damien Hutsemékers¹, Jean Manfroid¹, Emmanuël Jehin¹, Cyrielle Opitom², Rohan Rahatgaonkar⁴, Michele Bannister³, Juan Pablo Carvajal⁴, Rosemary Dorsey⁵, K. Aravind¹, Baltasar Luco⁴, Brian Murphy², Thomas H. Puzia⁴

¹ STAR, Institut d’Astrophysique et de Géophysique, Université de Liège, Allée du 6 Août 19c, 4000 Liège, Belgium

² Institute for Astronomy, University of Edinburgh, Royal Observatory, Edinburgh EH9 3HJ, United Kingdom

³ School of Physical and Chemical Sciences - Te Kura Matū, University of Canterbury, Private Bag 4800, Christchurch 8140, New Zealand

⁴ Institute of Astrophysics, Pontificia Universidad Católica de Chile, Av. Vicuña Mackenna 4860, 7820436 Macul, Santiago, Chile

⁵ Department of Physics, University of Helsinki, P.O. Box 64, 00014 Helsinki, Finland

Received ; accepted:

ABSTRACT

Emission lines of FeI and NiI are commonly found in the coma of Solar System comets, even at large heliocentric distances. These atoms are most likely released from the surface of the comet’s nucleus or from a short-lived parent. The presence of these lines in cometary spectra is unexpected because the surface blackbody equilibrium temperature is too low to allow the sublimation of refractory minerals containing these metals. These lines were also found in the interstellar comet 2I/Borisov, which has a NiI/FeI abundance ratio similar to that observed in Solar System comets. On average, this ratio is one order of magnitude higher than the solar Ni/Fe abundance ratio. Here, we report observations of the interstellar comet 3I/ATLAS, which were carried out with the ESO Very Large Telescope equipped with the UVES and X-shooter spectrographs. Spectra were obtained at heliocentric distances ranging from 3.14 to 1.85 au. NiI was detected at all epochs. FeI was only detected at heliocentric distances smaller than 2.64 au. We estimated the NiI and FeI production rates by comparing the observed line intensities with those produced by a dedicated fluorescence model. Comet 3I first exhibited extreme and unusual NiI/FeI abundance ratios during the initial stages of its activity. However, as its heliocentric distance decreased, this ratio became indistinguishable from those observed in Solar System comets and in comet 2I/Borisov. Comet 3I was found to be C₂-depleted, with a NiI/FeI abundance ratio finally consistent with other C₂-depleted comets. Nevertheless, comet 3I remains exceptional due to its high, total production rate of NiI and FeI, which is at least one order of magnitude larger than that of other comets. We interpreted these observations assuming that the NiI and FeI atoms were released through the sublimation of Ni(CO)₄ and Fe(CO)₅ carbonyls. This scenario provides a straightforward explanation for the asymmetric release of NiI and FeI atoms in the cometary coma and how it depends on the heliocentric distance. It also supports the presence of carbonyls in the cometary material.

Key words. Comets: general

1. Introduction

Numerous FeI and NiI emission lines have been identified in the spectra of about 20 Solar System comets observed in the last two decades at heliocentric distances (r_h) ranging from 0.68 to 3.25 au (Manfroid et al. 2021; Hutsemékers et al. 2021; Hmoudouch et al. 2025). The presence of these lines in cometary spectra at such distances from the Sun was unexpected because the surface blackbody equilibrium temperature is too low to allow the sublimation of silicate and sulfide minerals containing the metals. Furthermore, the mean abundance ratio NiI/FeI was found to be one order of magnitude higher than the solar ratio, and higher than the ratios estimated in the dust of 1P/Halley (Jessberger et al. 1988) and in the coma of the Sun-grazing comet Ikeya-Seki (Manfroid et al. 2021). Manfroid et al. (2021) advanced several mechanisms to explain these observations, in particular superheating of Ni-rich sulfides, possibly located in nanoparticles, and sublimation of organometallic com-

plexes, such as carbonyls (see also Bromley et al. 2021 and Rahatgaonkar et al. 2025).

Interstellar comets, with potentially different chemical compositions, offer a unique opportunity to better understand the origin of the NiI and FeI atoms observed in cometary comae. FeI and NiI were found in the interstellar comet 2I/Borisov (hereafter 2I) with a NiI/FeI abundance ratio similar to the Solar System comets (Guzik & Drahus 2021; Opitom et al. 2021). NiI was recently found in the interstellar comet 3I/ATLAS (hereafter 3I) at a heliocentric distance of 3.88 au, before the onset of CN and FeI (Rahatgaonkar et al. 2025). This could support an unusual composition of comet 3I, as is suggested by the very high CO₂/H₂O abundance ratio found by Cordiner et al. (2025).

In this work, we report the first detection of FeI emission lines in the coma of comet 3I at a heliocentric distance of 2.64 au. We measured the NiI/FeI abundance ratio at different heliocentric distances and compared it to the ratio observed in Solar System comets and comet 2I to determine whether comet 3I is unique. We show that the release of NiI and FeI atoms at large distances from the Sun can be explained by the sublimation of short-lived species, possibly carbonyls.

[★] Based on observations made with the ESO Very Large Telescope at the Paranal Observatory under programs 115.C-0282, 115.C-2317, and 2115.C-5030.

2. Observations and data reduction

Observations were carried out from August 12 to September 14, 2025, with the Very Large Telescope (VLT) at the European Southern Observatory (ESO), equipped with the UV-Visual Echelle Spectrograph (UVES¹). The standard settings 346+580 (dichroic 1), 390+580 (dichroic 1), and 437+860 (dichroic 2) were used. The blue settings centered at 346 nm, 390 nm, and 437 nm cover the spectral ranges 3030–3880 Å, 3260–4540 Å, and 3730–4990 Å, respectively. A nonstandard setting centered at 348 nm, corresponding to the spectral range 3100–3900 Å, was also used to simultaneously cover the regions containing the OH and CN bands. Most of the time, a 1.8''-wide slit was used, delivering a resolving power of about 35000. The observing circumstances are summarized in Table A.1. Raw frames were first processed to remove cosmic ray hits using the Python implementation of the “lacosmic” package (van Dokkum 2001; van Dokkum et al. 2012). The data were reduced with the UVES pipeline² to obtain wavelength- and flux-calibrated two-dimensional spectra. One-dimensional spectra were then extracted by integrating over the full slit length (Table A.3), using custom procedures. The scattered spectrum of the Sun (dust, twilight) was removed in the manner described in Manfroid et al. (2009).

We also considered the spectra obtained with the VLT X-shooter spectrograph³ (Vernet et al. 2011) and described in detail by Rahatgaonkar et al. (2025), in particular the UVB spectra obtained from July 23 to August 21, 2025, which contain the first detections of NiI lines in comet 3I. These observations were secured with a 1.6''-wide slit, providing a resolving power of about 3200. Another series of spectra, containing both the NiI and FeI lines, was obtained from September 20 to 25, 2025, with the same instrumental settings. The observing circumstances are summarized in Table A.2. All of these spectra were independently reduced in the present work. The X-shooter pipeline⁴ was used to obtain wavelength- and flux- calibrated two-dimensional spectra. Since the target was not always positioned in the middle of the 10''-long slit, the one-dimensional spectra were extracted over a shorter, 7.5''-long slit centered on the target. The scattered spectrum of the Sun was subtracted using the solar analog star HD150469, which was observed with the same settings as the comet (Rahatgaonkar et al. 2025).

3. FeI line detection and production rate measurements

While NiI lines were observed in the spectra obtained before August 28 and detected as far as 3.88 au (Rahatgaonkar et al. 2025, see also Table A.3), FeI lines were only detected in the spectra obtained on August 28 with UVES, and after that date when the comet was at $r_h \leq 2.64$ au. Some of the brightest FeI lines are shown in Fig. 1. After August 28, the lines steadily intensified, and new ones emerged (Figs. B.1 and B.2).

The intensities of unblended FeI and NiI emission lines were measured in the UVES and X-shooter spectra for each epoch,

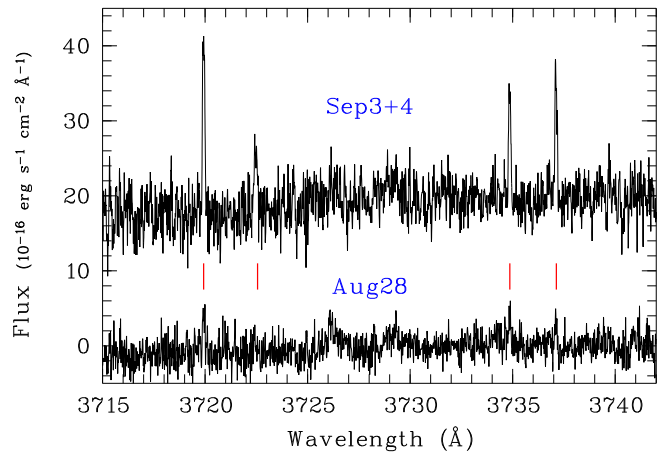


Fig. 1. Continuum-subtracted spectra of comet 3I obtained on August 28 and September 3+4 with UVES. Three narrow FeI lines were detected on August 28 in this spectral range, FeI $\lambda 3719.93\text{\AA}$ being the brightest iron line detected in our spectra. In the average spectrum obtained in September 3+4 (shifted vertically for clarity), the FeI lines are brighter, and four of them were detected (as is indicated by the vertical red lines). Broad emission features due to background [OII] emission at 3727 Å and 3729 Å are also observed.

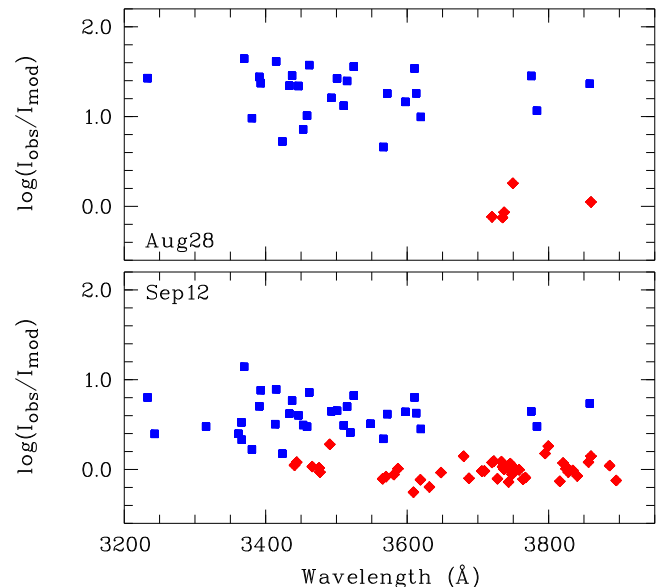


Fig. 2. Ratio $\log_{10}(I_{\text{obs}}/I_{\text{mod}})$ for the FeI (red diamonds) and NiI (blue squares) lines measured in comet 3I for observations secured with UVES on August 28 (top) and September 12 (bottom). I_{obs} represents the observed line intensities and I_{mod} the intensities computed with the fluorescence model. $I_{\text{obs}}/I_{\text{mod}}$ is proportional to the column density of the atoms (Manfroid et al. 2021). The separation between the mean values computed for NiI and FeI gives the NiI/FeI abundance ratio. The ratios have been shifted on the y axis so that the mean value of $\log_{10}(I_{\text{obs}}/I_{\text{mod}})$ is zero for FeI.

and compared to the intensities computed with a dedicated fluorescence model to derive the FeI and NiI column densities. This model, described in detail in Manfroid et al. (2021), considers a large number of transitions and atomic levels for both the FeI and NiI atoms. Since FeI and NiI lines are also present in absorption in the solar light that irradiates the cometary atmosphere, the excitation can strongly depend on the Doppler shift between the comet and the solar spectra. Therefore, the high-resolution struc-

¹ UVES User Manual, VLT-MAN-ESO-13200-1825, <https://www.eso.org/sci/facilities/paranal/instruments.html>

² UVES Pipeline User Manual, VLT-MAN-ESO-19500-2965, <https://www.eso.org/sci/software.html>

³ X-shooter User Manual, ESO-270545, <https://www.eso.org/sci/facilities/paranal/instruments.html>

⁴ X-shooter Pipeline User Manual, VLT-MAN-ESO-14650-4840, <https://www.eso.org/sci/software.html>

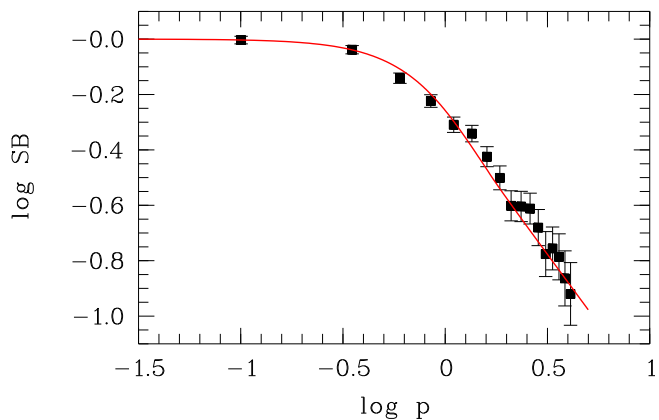


Fig. 3. Spatial profile of the brightest NiI line ($\lambda 3458\text{\AA}$) observed with UVES on September 4. The measured surface brightness (SB; normalized to one at the photocenter) is plotted as a function of the projected nucleocentric distance, p , in arcsec. The red line represents $\text{SB} \propto p^{-1}$ convolved with a 1.5'' full-width-at-half-maximum Gaussian to account for the seeing and tracking imperfections.

ture of the solar spectrum and the relative velocity between the comet and the Sun must be considered.

A comparison of observed and computed line intensities for FeI and NiI is shown in Fig. 2, for two epochs. The ratio $I_{\text{obs}}/I_{\text{mod}}$ gives the atomic column density (Manfroid et al. 2021). Although there is clearly some dispersion between the individual measurements, the average of the intensity ratios is well defined for both atomic species. The difference of the average values gives the NiI/FeI abundance ratio, which is clearly higher on August 28 than on September 12 (see also Table A.3).

One important characteristic of the FeI and NiI emission lines is their short spatial extent. In spectra obtained for comets 103P/Hartley2 and 46P at geocentric distances of 0.17 and 0.09 au, respectively, the surface brightness was found to be inversely proportional to the projected distance from the nucleus, p (Manfroid et al. 2021; Hutsemékers et al. 2021). Such a spatial profile indicates that the FeI and NiI atoms originate at small nucleocentric distances, either directly ejected from the surface of the nucleus or released from a short-lived parent. As is shown in Fig. 3, a similar profile is observed for comet 3I.

Assuming that the emission line surface brightness decreases as p^{-1} for both NiI and FeI, production rates were computed from the column densities according to the formulae given in Manfroid et al. (2021). We assumed a constant ejection velocity, $v = 0.85 r_h^{-0.5} \text{ km s}^{-1}$ (Cochran & Schleicher 1993). The resulting production rates and abundance ratios are given in Table A.3, together with the number of lines used in the analysis. The NiI production rates measured for the first X-shooter dataset are in good agreement with those reported in Rahatgaonkar et al. (2025), although they are slightly smaller due a more conservative measurement of the line intensities. Since NiI and FeI were simultaneously observed, abundance ratios can be derived from either column densities or production rates.

The production rates of OH, CN, and C₂ were also estimated as in Manfroid et al. (2021), using the OH(0-0) band at 3090 Å, the CN(0-0) band at 3870 Å, and the C₂ band at 5140 Å. The rates were derived using the fluorescence efficiencies and Haser scalelengths from Schleicher & A'Hearn (1988), Cochran & Schleicher (1993), A'Hearn et al. (1995), and Schleicher (2010), with a parent and daughter velocity of $0.85 r_h^{-0.5} \text{ km s}^{-1}$ (Cochran & Schleicher 1993). These production rates are given in Table A.4.

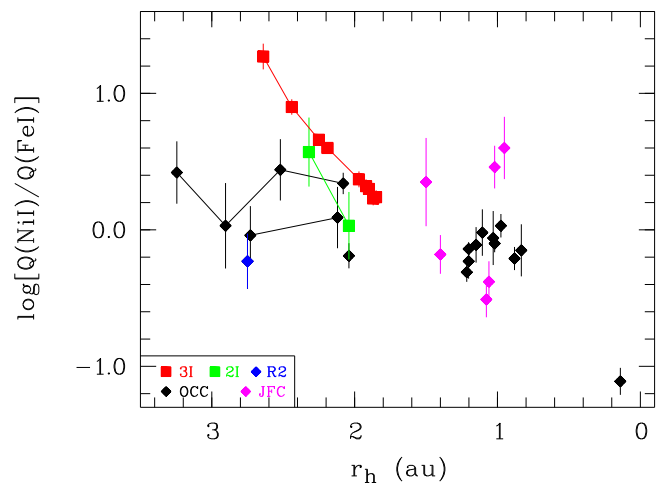


Fig. 4. $Q(\text{NiI})/Q(\text{FeI})$ as a function of the heliocentric distance, r_h , for interstellar and Solar System comets. The measurements obtained at different heliocentric distances are not averaged and shown individually for comets 3I (9 values, pre-perihelion), 2I (2 values, post-perihelion), C/2001 P1 (4 values, pre-perihelion), and C/2017 K2 (2 values, pre-perihelion). The comet with the smallest $Q(\text{NiI})/Q(\text{FeI})$ ratio is C/1965 S1(Ikeya-Seki) observed at 0.14 au from the Sun. The solar Ni/Fe abundance ratio is equal, in logarithm, to -1.25 ± 0.04 (Asplund et al. 2009).

4. Comparison of comet 3I to other comets

We compared the NiI and FeI production rates and the NiI/FeI abundance ratio measured in comet 3I to the same quantities evaluated in other comets (Figs. 4 to 6). The NiI and FeI production rates were measured in approximately 20 comets based on UVES observations (except comet C/1996 B2 Hyakutake). The data are taken from Manfroid et al. (2021) and Hutsemékers et al. (2021), as are the production rates of C₂ and CN. These measurements include those obtained for the interstellar comet 2I (Opitom et al. 2021). We also added the data of comet C/2017 K2, which was recently investigated by Hmida et al. (2025). Unless otherwise stated, when more than one measurement is available for a given comet, we used the simple average, with errors computed from the individual measurements. For comet 3I, however, we show the individual measurements separately. Solar System comets were classified into two broad categories: Jupiter-family comets (JFCs) and Oort-cloud comets (OCCs). For subgroup definitions and the identification of the individual comets in the plots, we refer to Manfroid et al. (2021) and Hutsemékers et al. (2021). In the plots, we emphasize the measurements of the interstellar comet 2I and of the unusual N₂-rich Solar System comet C/2016 R2 (Opitom et al. 2019).

Figure 4 shows $Q(\text{NiI})/Q(\text{FeI})$ as a function of the comet heliocentric distance. No correlation was found between $Q(\text{NiI})/Q(\text{FeI})$ and r_h for the Solar System comets (Manfroid et al. 2021). For some comets, $Q(\text{NiI})/Q(\text{FeI})$ was measured at different heliocentric distances, higher than 3 au for C/2000 P1, and it was found to be constant within the error bars. However, comet 3I breaks the rule by showing an extremely high $Q(\text{NiI})/Q(\text{FeI})$ ratio at $r_h \approx 2.64$ au and a rapid decrease with decreasing r_h . After one month, at a heliocentric distance of around 2 au, its value became comparable to that of the other Solar System comets. The unexpected behavior of $Q(\text{NiI})/Q(\text{FeI})$ in comet 3I can be clearly seen thanks to the small errors of the measurements. Therefore, we cannot exclude the possibility that other comets exhibited the same behavior, but were simply not regu-

larly monitored with a signal-to-noise ratio good enough to detect it. The two $Q(\text{NiI})/Q(\text{FeI})$ measurements in the interstellar comet 2I seem to show a trend with the heliocentric distance. However, the ratios are equal within the error bars, so the inferred trend is not statistically significant. Therefore, we only considered the average value of $Q(\text{NiI})/Q(\text{FeI})$ for comet 2I in the following.

Figure 5 shows the $Q(\text{NiI})/Q(\text{FeI})$ ratio as a function of the total production rate of the NiI and FeI atoms. On average, OCCs have higher $Q(\text{FeI}+\text{NiI})$ rates than JFCs, while the latter show a larger dispersion of the $Q(\text{NiI})/Q(\text{FeI})$ ratio (Hutsemékers et al. 2021). In this plot, comet 3I is clearly exceptional. When the $Q(\text{NiI})/Q(\text{FeI})$ ratio becomes similar to that observed in the other comets, the total $Q(\text{FeI}+\text{NiI})$ production rate in comet 3I is one order of magnitude larger than the highest value measured in Solar System comets at heliocentric distance smaller than 1.85 au. Comet 2I, on the other hand, is just ordinary, with a total $Q(\text{FeI}+\text{NiI})$ production rate two orders of magnitude smaller than that of comet 3I, at a comparable heliocentric distance. It is also interesting to note that, at $r_h \simeq 2.75$ au, $Q(\text{FeI}+\text{NiI})$ in comet C/2016 R2 was a factor of about 2.5 times larger than in comet 3I. However, unlike comet 3I, the metal production in comet C/2016 R2 was dominated by FeI and not NiI. Unfortunately, comet C/2016 R2 was not observed at other heliocentric distances.

Figure 6 shows the correlation between $Q(\text{NiI})/Q(\text{FeI})$ and $Q(\text{C}_2)/Q(\text{CN})$ previously established for the Solar System comets (Hutsemékers et al. 2021). Given the variation of $Q(\text{NiI})/Q(\text{FeI})$ in comet 3I, one might thus wonder how it fits the relationship. Ignoring the leftmost data point, where $Q(\text{CN})$ temporarily increases faster than $Q(\text{C}_2)$, $\log[Q(\text{C}_2)/Q(\text{CN})]$ for comet 3I consistently lies between -0.5 and -0.3 at all heliocentric distances (epochs). With $\log[Q(\text{C}_2)/Q(\text{CN})] \lesssim -0.13$ (Bair & Schleicher 2025), comet 3I can thus be confidently classified as a C_2 -depleted comet, though not as strongly depleted as is reported by Salazar Manzano et al. (2025). Comet 3I perfectly fits the correlation between $Q(\text{NiI})/Q(\text{FeI})$ and $Q(\text{C}_2)/Q(\text{CN})$ once $\log[Q(\text{NiI})/Q(\text{FeI})]$ stabilizes around 0.3 when the comet was at $r_h \simeq 2$ au. While within this correlation, the properties of comet 3I appear very similar to those of comet 2I.

It is also interesting to note that, between $r_h = 2.64$ and 2.19 au, $\log[Q(\text{CN})/Q(\text{OH})]$ in comet 3I is in the range of -1.8 to -2.2 . These values are consistent with those measured for Solar System comets (A'Hearn et al. 1995), though they are at the higher end. However, our measurements are significantly higher than the ratio of $\log[Q(\text{CN})/Q(\text{OH})] \simeq -3.1$ reported by Xing et al. (2025) when comet 3I was at 2.9 au.

In summary, comet 3I exhibits an extremely high $Q(\text{NiI})/Q(\text{FeI})$ ratio at the onset of FeI. Later, this ratio decreases regularly and, at $r_h \simeq 2$ au, becomes indistinguishable from the ratio measured in other Solar System comets and the interstellar comet 2I. On the other hand, the total production rate of NiI and FeI atoms, which was not exceptional at $r_h \simeq 3$ au, strongly increases and, at $r_h \simeq 2$ au, becomes more than one order of magnitude larger than that of other comets observed at comparable or smaller heliocentric distances.

5. Discussion: The origin of NiI and FeI atoms

The expected blackbody equilibrium temperature, T , (in Kelvin) of the cometary surface is approximately given by

$$T \simeq 280 r_h^{-1/2}, \quad (1)$$

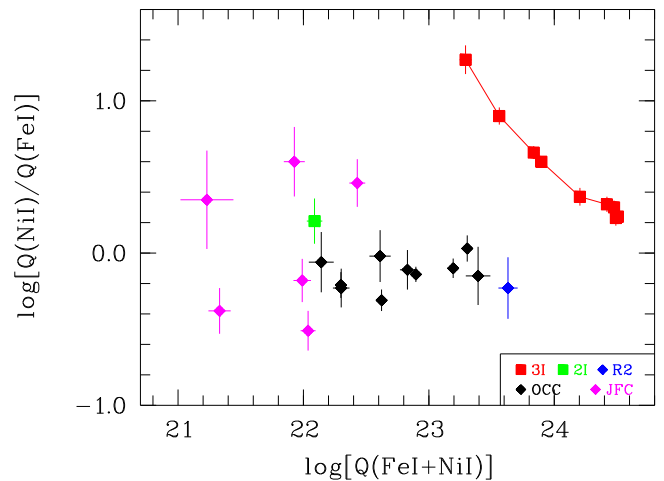


Fig. 5. $Q(\text{NiI})/Q(\text{FeI})$ as a function of the total production rate $Q(\text{FeI}+\text{NiI})$. Comet 3I was observed in the range 2.64 – 1.85 au. Solar System comets with $r_h > 1.85$ au are not shown, except comet C/2016 R2, which was observed at 2.75 au. Comet 2I was observed at 2.18 ± 0.14 au.

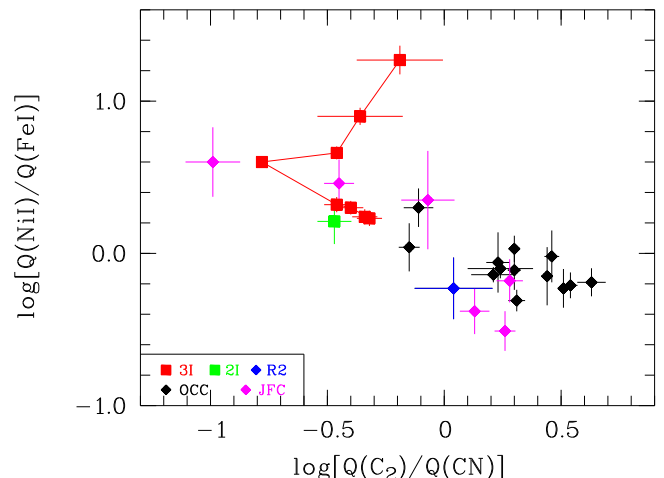


Fig. 6. $Q(\text{NiI})/Q(\text{FeI})$ as a function of the production rate ratio $Q(\text{C}_2)/Q(\text{CN})$.

where r_h is in astronomical units (Manfroid et al. 2021; Guzik & Drahus 2021; Puzia et al. 2025). At the distances at which the comets were observed, this temperature is far too low to vaporize silicate, sulfide, and metallic grains that contain NiI and FeI atoms. Therefore, the presence of NiI and FeI atoms in cometary comae is extremely puzzling. Several hypotheses have been proposed to explain the presence of the NiI and FeI atoms at low surface temperatures as well as the high NiI/FeI abundance ratio, much higher than the Solar System value. These scenarios were first presented by Manfroid et al. (2021), and discussed further by Bromley et al. (2021) and Rahatgaonkar et al. (2025). In particular, Manfroid et al. (2021) proposed that the NiI and FeI atoms could be released from $\text{Ni}(\text{CO})_4$ and $\text{Fe}(\text{CO})_5$ carbonyls, which are characterized by very low sublimation temperatures. The smaller sublimation temperature of $\text{Ni}(\text{CO})_4$ with respect to $\text{Fe}(\text{CO})_5$ could also explain the high NiI/FeI ratios observed at low surface temperatures. The carbonyl scenario, although appealing, predicts a NiI/FeI ratio that strongly depends on the temperature, and thus on the heliocentric distance. Unfortunately, such a dependence was not observed in the sample of Solar System comets studied by Manfroid et al. (2021).

On the contrary, comet 3I exhibits significant variation in its NiI/FeI abundance ratio as a function of the heliocentric distance, enabling us to further explore this scenario. Rahatgaonkar et al. (2025) already noticed that the production rate of NiI changes much faster with the heliocentric distance than can be explained by purely radiative processes.

Bromley et al. (2021) showed that the photodissociation of $\text{Ni}(\text{CO})_4$ and $\text{Fe}(\text{CO})_5$ into atomic NiI and FeI is very fast, with similar rates for both carbonyls, and occurs at nucleocentric distances consistent with the observed spatial distributions of the atoms. Therefore, the NiI and FeI production rates can be directly compared to the carbonyl sublimation rates. The sublimation rates of $\text{Ni}(\text{CO})_4$ and $\text{Fe}(\text{CO})_5$ were computed as a function of the temperature as in Manfroid et al. (2021). Then, they were expressed as a function of r_h using Eq. 1. The ratio of the sublimation rates was finally corrected by assuming an intrinsic cometary Ni/Fe abundance ratio equal to the Solar System Ni/Fe abundance ratio⁵, $\log_{10}(\text{Ni}/\text{Fe}) = -1.25$ (Asplund et al. 2009).

Figure 7 shows the variation in $Q(\text{NiI})$ between 3.78 and 1.85 au, and the variation in $Q(\text{FeI})$ between 2.64 au and 1.85 au. The solid curves represent the production rates of NiI and FeI computed from the sublimation rates of $\text{Ni}(\text{CO})_4$ and $\text{Fe}(\text{CO})_5$, which were multiplied by the effective emitting area of each species. The sublimation rates were computed assuming that the comet was at the equilibrium temperature at each heliocentric distance (Eq. 1). The effective emitting area was estimated empirically by shifting vertically (in logarithm) the sublimation rate curves (in molecules $\text{m}^{-2} \text{ s}^{-1}$) to match the observed production rates (in atoms s^{-1}). The effective emitting areas were found to be equal to 1.6 m^2 for both $\text{Ni}(\text{CO})_4$ and $\text{Fe}(\text{CO})_5$. This area is small, as is expected for minor species. However, its value should be interpreted with caution given the basic model. The $\text{Fe}(\text{CO})_5$ sublimation model nicely reproduces the variation in $Q(\text{FeI})$ with the heliocentric distance. For NiI, the global trend is reproduced, indicating that carbonyl sublimation begins very early. However, the increase in $Q(\text{NiI})$ with the heliocentric distance is less steep than the simple sublimation model predicts. This suggests that the temperature of the NiI-emitting regions may differ from the blackbody equilibrium temperature. Indeed, a reasonable fit can be obtained using the ad hoc relation $T = 237 r_h^{-1/3}$. As the comet approaches the Sun, more material is ejected, fractures form, and the temperature can deviate significantly from the blackbody equilibrium temperature, at least in localized regions (e.g., Prialnik et al. 2004; Groussin et al. 2013; Höfner et al. 2017). The different behavior of NiI and FeI with respect to the simple sublimation model could also indicate that these atoms are partially released from different subregions.

Figure 8 shows the ratio of the sublimation rates of $\text{Ni}(\text{CO})_4$ and $\text{Fe}(\text{CO})_5$ computed as a function of r_h according to Eq. 1, together with the NiI/FeI abundance ratios measured in interstellar and Solar System comets. As before, the ratio of the sublimation rates is adjusted to account for the cometary intrinsic Ni/Fe abundance ratio, which is assumed to be equal to the Solar System value. Although the model is extremely basic, the computed ratio of the sublimation rates of $\text{Ni}(\text{CO})_4$ to $\text{Fe}(\text{CO})_5$ (solid curve) reproduces the NiI/FeI ratio observed in several comets within a factor 2-3, though not in all of them. In particular, it accurately reproduces the ratio observed in comet 3I at the onset of FeI at $r_h \simeq 2.64$ au. However, the rapid decrease in the NiI/FeI ratio with r_h does not follow the theoretical curve computed under

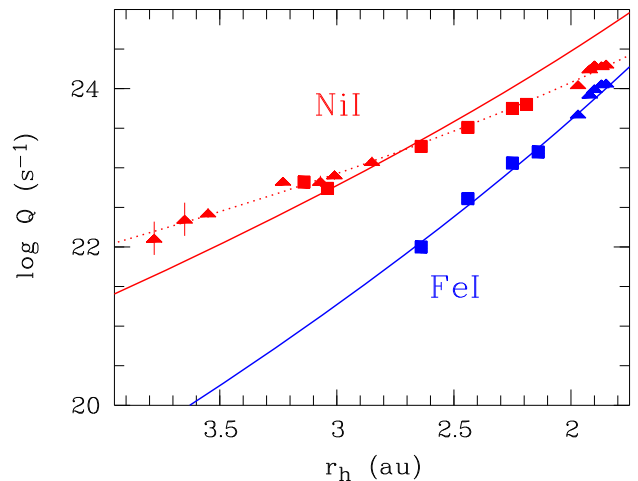


Fig. 7. $Q(\text{NiI})$ and $Q(\text{FeI})$ production rates in comet 3I as a function of the heliocentric distance. Squares represent UVES measurements and triangles X-shooter measurements. The curves show the production rates of NiI (in red) and FeI (in blue), which were obtained by multiplying the sublimation rates of the $\text{Ni}(\text{CO})_4$ and $\text{Fe}(\text{CO})_5$ carbonyls by the effective emitting area of each species (see text). For the solid curves, the sublimation rates were computed assuming $T = 280 r_h^{-1/2}$. For the dotted red curve, the sublimation rate was computed assuming $T = 237 r_h^{-1/3}$ for $\text{Ni}(\text{CO})_4$.

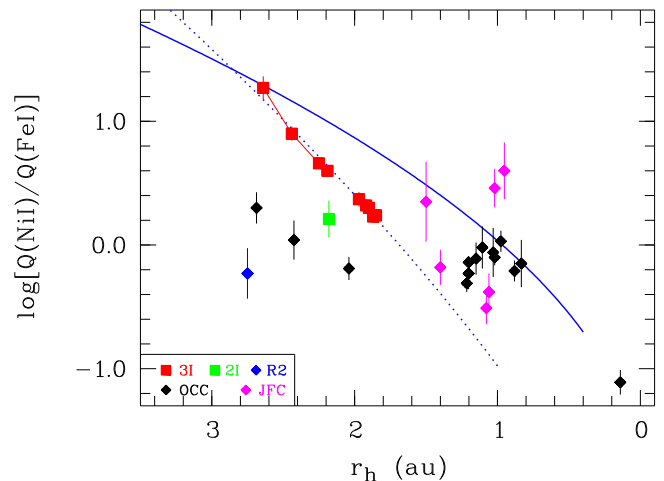


Fig. 8. $Q(\text{NiI})/Q(\text{FeI})$ as a function of the heliocentric distance for interstellar and Solar System comets. The solid curve represents the ratio of the sublimation rates of the $\text{Ni}(\text{CO})_4$ and $\text{Fe}(\text{CO})_5$ carbonyls computed assuming $T = 280 r_h^{-1/2}$ for both $\text{Ni}(\text{CO})_4$ and $\text{Fe}(\text{CO})_5$. The dotted line represents the sublimation rate ratio assuming $T = 237 r_h^{-1/3}$ for the $\text{Ni}(\text{CO})_4$ emitting region, as in Fig. 7.

the hypothesis that the comet remains at the equilibrium temperature. Assuming a different temperature dependence, such as $T = 237 r_h^{-1/3}$, allows us to reproduce the NiI/FeI variation (dotted curve). Therefore, the ratio of the carbonyl sublimation rates at the equilibrium temperature should be considered as an upper limit of the observed NiI/FeI ratios. The lack of correlation between the NiI/FeI ratio and r_h for Solar System comets may be due to the dispersion of their temperatures and surface properties at a given heliocentric distance.

Although incomplete, this scenario provides a straightforward explanation for the release of NiI and FeI atoms in comets and suggests the presence of carbonyls in the cometary material. However, it is clear that there is more to the story. The NiI/FeI

⁵ It should be emphasized that the Ni/Fe abundance ratio in the cometary material (ices and dust) differs from the abundance ratio of the NiI and FeI atoms in the coma, which depends on the sublimation rates.

ratio is also connected to the carbon content, as is shown by the relationship between the NiI/FeI and C₂/CN ratios (Fig. 6). Since the C₂ depletion is primordial rather than evolutionary (Bair & Schleicher 2025), the NiI/FeI abundance ratio could also be primordial in part. Comet 3I exhibits a CO₂/H₂O abundance ratio of 7.6 at $r_h = 3.3$ au, which is higher than that of Solar System comets, and a CO/H₂O ratio of 1.7, which is consistent with other cometary observations (Cordiner et al. 2025), including with those of comet 2I, which exhibits CO/H₂O ratios ranging from 1.3 to 1.6 at 2.0 au (Bodewits et al. 2020). Comet C/2016 R2 exhibits more extreme abundance ratios: CO₂/H₂O ≈ 30 and CO/H₂O ≈ 300 at $r_h = 2.8$ au (McKay et al. 2019). The high Q(FeI+NiI) production rates observed in comets 3I and C/2016 R2 at approximately 2-3 au (Sect. 4 and Fig. 5) could be related to the high abundance of CO₂, CO, or both. As is suggested by Cordiner et al. (2025), the high CO₂/H₂O measured in comet 3I could be due to a lower temperature of the cometary surface, which would also affect the metal production. On the other hand, when more CO₂ and CO molecules are available in the cometary material, more NiI and FeI atoms could be incorporated into carbonyls during the comet formation, so that more NiI and FeI atoms are finally produced when these carbonyls sublimate. A better understanding of carbonyl formation in various chemical environments is needed, in particular to determine whether an initial Ni(CO)₄ / Fe(CO)₅ asymmetry can already be produced during the comet formation, depending on the carbon oxide content. Interestingly, Q(FeI+NiI) is dominated by NiI in comet 3I (Fig. 5), which has a high CO₂/CO ratio, while Q(FeI+NiI) is dominated by FeI in comet C/2016 R2, which, on the contrary, has a high CO/CO₂ ratio. Finally, it is worth noting that other mechanisms, such as superheating of nanograins, could also contribute to the release of NiI and FeI atoms from refractory material. However such mechanisms cannot fully explain the observed NiI/FeI ratios (see Manfroid et al. 2021). For Sun-grazing comets, complete vaporization of refractory grains occurs, leading to a solar NiI/FeI abundance ratio.

6. Conclusions

Since the beginning of its activity, the interstellar comet 3I/ATLAS has been regularly observed with UVES and X-shooter. These observations have provided an unprecedented dataset revealing the evolution of the NiI and FeI emission lines with heliocentric distance. During the initial stages of its activity, comet 3I exhibited extreme and unusual NiI/FeI abundance ratios. However, as its heliocentric distance decreased, the ratio became indistinguishable from those observed in Solar System comets and in the interstellar comet 2I/Borisov. Comet 3I was found to be C₂-depleted, with a NiI/FeI abundance ratio finally consistent with other C₂-depleted comets. Nevertheless, comet 3I remains exceptional due to its high total production rate of NiI and FeI, which is at least one order of magnitude larger than that of other comets. This enhanced metal production is possibly related to other chemical anomalies, such as the high CO₂/H₂O abundance ratio.

The NiI and FeI production rates, as well as their variations with heliocentric distance, are interpreted within the context of the sublimation of Ni(CO)₄ and Fe(CO)₅ carbonyls. This scenario provides a straightforward explanation for the asymmetric release of NiI and FeI atoms in the cometary coma and how it depends on heliocentric distance. Post-perihelion observations of NiI and FeI would be helpful to confirm the findings of this paper and clarify the trend with the heliocentric distance, in particular to discriminate between genuine variation with the helio-

centric distance and effects due to processing of the outer layers of the nucleus.

Acknowledgements. We thank the referee for comments that helped significantly improve the manuscript. DH and EJ are Research Directors at the F.R.S-FNRS. JM is honorary Research Director at the F.R.S-FNRS. THP, RR, JPC, BL gratefully acknowledge support from the National Agency for Research and Development (ANID) under the following grants: CATA-Basal FB210003 and Beca de Doctorado Nacional (R.R. and J.P.C.). R.C.D. acknowledges support from grant #361233 awarded by the Research Council of Finland to M. Granvik.

References

A'Hearn, M. F., Millis, R. C., Schleicher, D. O., Osip, D. J., & Birch, P. V. 1995, *Icarus*, 118, 223
 Asplund, M., Grevesse, N., Sauval, A. J., & Scott, P. 2009, *ARA&A*, 47, 481
 Bair, A. N. & Schleicher, D. G. 2025, *The Planetary Science Journal*, 6, 248
 Bodewits, D., Noonan, J. W., Feldman, P. D., et al. 2020, *Nature Astronomy*, 4, 867
 Bromley, S. J., Neff, B., Loch, S. D., et al. 2021, *Planetary Science Journal*, 2, 228
 Cochran, A. L. & Schleicher, D. G. 1993, *Icarus*, 105, 235
 Cordiner, M. A., Roth, N. X., Kelley, M. S. P., et al. 2025, *ApJ*, 991, L43
 Groussin, O., Sunshine, J. M., Feaga, L. M., et al. 2013, *Icarus*, 222, 580
 Guzik, P. & Drahus, M. 2021, *Nature*, 593, 375
 Hmoudouch, S., Jehin, E., Lippi, M., et al. 2025, *A&A*, 701, A61
 Höfner, S., Vincent, J. B., Blum, J., et al. 2017, *A&A*, 608, D
 Hutsemékers, D., Manfroid, J., Jehin, E., Opitom, C., & Moulane, Y. 2021, *A&A*, 652, L1
 Jessberger, E. K., Christoforidis, A., & Kissel, J. 1988, *Nature*, 332, 691
 Manfroid, J., Hutsemékers, D., & Jehin, E. 2021, *Nature*, 593, 372
 Manfroid, J., Jehin, E., Hutsemékers, D., et al. 2009, *A&A*, 503, 613
 McKay, A. J., DiSanti, M. A., Kelley, M. S. P., et al. 2019, *AJ*, 158, 128
 Opitom, C., Hutsemékers, D., Jehin, E., et al. 2019, *A&A*, 624, A64
 Opitom, C., Jehin, E., Hutsemékers, D., et al. 2021, *A&A*, 650, L19
 Prialnik, D., Benkhoff, J., & Podolak, M. 2004, in *Comets II*, ed. M. C. Festou, H. U. Keller, & H. A. Weaver, 359
 Puzia, T. H., Rahatgaonkar, R., Carvajal, J. P., Nayak, P. K., & Luco, B. 2025, *ApJ*, 990, L27
 Rahatgaonkar, R., Carvajal, J. P., Puzia, T. H., et al. 2025, *ApJ*, 995, L34
 Salazar Manzano, L. E., Lin, H. W., Taylor, A. G., et al. 2025, *ApJ*, 993, L23
 Schleicher, D. G. 2010, *AJ*, 140, 973
 Schleicher, D. G. & A'Hearn, M. F. 1988, *ApJ*, 331, 1058
 van Dokkum, P. G. 2001, *PASP*, 113, 1420
 van Dokkum, P. G., Bloom, J., & Tewes, M. 2012, *Astrophysics Source Code Library*, ascl:1207.005
 Vernet, J., Dekker, H., D'Odorico, S., et al. 2011, *A&A*, 536, A105
 Xing, Z., Oset, S., Noonan, J., & Bodewits, D. 2025, *ApJ*, 991, L50

Appendix A: Tables

Table A.1. Observing circumstances: UVES.

| Date yyyy-mm-dd | r_h au | \dot{r}_h km s $^{-1}$ | Δ au | $\dot{\Delta}$ km s $^{-1}$ | Settings | w_B/w_R '' | h_B/h_R '' |
|--------------------|-------------|-----------------------------|----------------|--------------------------------|----------|-----------------|-----------------|
| 2025-08-12 | 3.14 | -55.3 | 2.69 | -15.4 | 346+580 | 1.8/0.6 | 9.5/11.5 |
| 2025-08-15 | 3.04 | -54.9 | 2.66 | -13.3 | 390+580 | 0.6/0.6 | 7.5/11.5 |
| 2025-08-28 | 2.64 | -52.9 | 2.59 | -6.6 | 348+580 | 1.8/0.6 | 9.5/11.5 |
| 2025-08-28 | 2.64 | -52.9 | 2.59 | -6.6 | 437+860 | 1.8/0.6 | 9.5/11.0 |
| 2025-09-03 | 2.46 | -51.6 | 2.57 | -4.8 | 348+580 | 1.8/1.2 | 9.5/11.5 |
| 2025-09-03 | 2.46 | -51.6 | 2.57 | -4.8 | 437+860 | 1.8/1.2 | 9.5/11.0 |
| 2025-09-04 | 2.43 | -51.3 | 2.57 | -4.6 | 348+580 | 1.8/1.2 | 9.5/11.5 |
| 2025-09-04 | 2.43 | -51.3 | 2.57 | -4.6 | 437+860 | 1.8/1.2 | 9.5/11.0 |
| 2025-09-10 | 2.25 | -49.5 | 2.55 | -3.7 | 348+580 | 1.8/1.2 | 9.5/11.5 |
| 2025-09-11 | 2.22 | -49.2 | 2.55 | -3.7 | 437+860 | 1.8/1.2 | 9.5/11.0 |
| 2025-09-12 | 2.19 | -48.8 | 2.55 | -3.6 | 348+580 | 1.8/1.2 | 9.5/11.5 |
| 2025-09-14 | 2.14 | -48.1 | 2.54 | -3.6 | 437+860 | 1.8/1.2 | 9.5/11.0 |

Table A.2. Observing circumstances: X-shooter.

| Date yyyy-mm-dd | r_h au | \dot{r}_h km s $^{-1}$ | Δ au | $\dot{\Delta}$ km s $^{-1}$ | w_B/h_B '' |
|--------------------|-------------|-----------------------------|----------------|--------------------------------|-----------------|
| 2025-07-23 | 3.78 | -56.8 | 2.96 | -32.5 | 1.6/11.0 |
| 2025-07-27 | 3.65 | -56.6 | 2.89 | -28.7 | 1.6/11.0 |
| 2025-07-30 | 3.55 | -56.4 | 2.84 | -26.0 | 1.6/11.0 |
| 2025-08-09 | 3.23 | -55.6 | 2.72 | -17.6 | 1.6/11.0 |
| 2025-08-14 | 3.07 | -55.0 | 2.67 | -14.0 | 1.6/11.0 |
| 2025-08-16 | 3.01 | -54.8 | 2.65 | -12.7 | 1.6/11.0 |
| 2025-08-21 | 2.85 | -54.1 | 2.62 | -9.7 | 1.6/11.0 |
| 2025-09-20 | 1.97 | -45.4 | 2.53 | -3.9 | 1.6/11.0 |
| 2025-09-22 | 1.92 | -44.3 | 2.52 | -4.2 | 1.6/11.0 |
| 2025-09-23 | 1.90 | -43.7 | 2.52 | -4.4 | 1.6/11.0 |
| 2025-09-24 | 1.87 | -43.1 | 2.52 | -4.5 | 1.6/11.0 |
| 2025-09-25 | 1.85 | -42.5 | 2.52 | -4.7 | 1.6/11.0 |

Notes. In Tables A.1 and A.2, r_h and Δ are the heliocentric and geocentric distances of the comet. \dot{r}_h and $\dot{\Delta}$ are the corresponding velocities. w_B , w_R , h_B , and h_R refer to the blue/red slit width and height, respectively.

Table A.3. FeI and NiI production rates, and their ratio.

| Date yyyy-mm-dd | r_h au | n _{lines} FeI / NiI | $\log_{10} Q(\text{FeI})$ s ⁻¹ | $\log_{10} Q(\text{NiI})$ s ⁻¹ | $\log_{10} [Q(\text{NiI})/Q(\text{FeI})]$ | Instrument |
|--------------------|-------------|---------------------------------|--|--|---|------------|
| 2025-07-23 | 3.78 | - / 2 | - | 22.11 ± 0.21 | - | X-shooter |
| 2025-07-27 | 3.65 | - / 2 | - | 22.35 ± 0.21 | - | X-shooter |
| 2025-07-30 | 3.55 | - / 4 | - | 22.43 ± 0.06 | - | X-shooter |
| 2025-08-09 | 3.23 | - / 3 | - | 22.83 ± 0.02 | - | X-shooter |
| 2025-08-12 | 3.14 | - / 20 | < 21.83 | 22.82 ± 0.06 | > 0.99 | UVES |
| 2025-08-14 | 3.07 | - / 11 | - | 22.83 ± 0.07 | - | X-shooter |
| 2025-08-15 | 3.04 | - / 14 | < 22.14 | 22.74 ± 0.08 | > 0.60 | UVES |
| 2025-08-16 | 3.01 | - / 12 | - | 22.91 ± 0.06 | - | X-shooter |
| 2025-08-21 | 2.85 | - / 14 | - | 23.08 ± 0.06 | - | X-shooter |
| 2025-08-28 | 2.64 | 5 / 28 | 22.00 ± 0.08 | 23.27 ± 0.05 | 1.27 ± 0.10 | UVES |
| 2025-09-3/4 | 2.44 | 17 / 36 | 22.61 ± 0.04 | 23.51 ± 0.04 | 0.90 ± 0.06 | UVES |
| 2025-09-10 | 2.25 | 42 / 36 | 23.06 ± 0.03 | 23.75 ± 0.03 | 0.66 ± 0.04 | UVES |
| 2025-09-12 | 2.19 | 46 / 37 | 23.20 ± 0.02 | 23.80 ± 0.03 | 0.60 ± 0.04 | UVES |
| 2025-09-20 | 1.97 | 11 / 18 | 23.68 ± 0.03 | 24.05 ± 0.05 | 0.37 ± 0.06 | X-shooter |
| 2025-09-22 | 1.92 | 16 / 18 | 23.93 ± 0.03 | 24.25 ± 0.04 | 0.32 ± 0.05 | X-shooter |
| 2025-09-23 | 1.90 | 21 / 18 | 24.00 ± 0.02 | 24.30 ± 0.04 | 0.30 ± 0.05 | X-shooter |
| 2025-09-24 | 1.87 | 18 / 20 | 24.06 ± 0.03 | 24.29 ± 0.04 | 0.23 ± 0.05 | X-shooter |
| 2025-09-25 | 1.85 | 16 / 20 | 24.07 ± 0.03 | 24.31 ± 0.04 | 0.24 ± 0.05 | X-shooter |

Table A.4. OH, CN, and C₂ production rates.

| Date yyyy-mm-dd | r_h au | $\log_{10} Q(\text{OH})$ s ⁻¹ | $\log_{10} Q(\text{CN})$ s ⁻¹ | $\log_{10} Q(\text{C}_2)$ s ⁻¹ | Instrument |
|--------------------|-------------|---|---|--|------------|
| 2025-08-12 | 3.14 | - | 24.2 ± 0.3 | - | UVES |
| 2025-08-15 | 3.04 | - | 24.59 ± 0.05 | - | UVES |
| 2025-08-28 | 2.64 | 26.58 ± 0.04 | 24.79 ± 0.04 | 24.6 ± 0.2 | UVES |
| 2025-09-3/4 | 2.44 | 26.79 ± 0.02 | 24.96 ± 0.03 | 24.6 ± 0.2 | UVES |
| 2025-09-10 | 2.25 | 27.24 ± 0.13 | 25.03 ± 0.01 | 24.57 ± 0.02 | UVES |
| 2025-09-11 | 2.22 | - | 25.34 ± 0.01 | - | UVES |
| 2025-09-12 | 2.19 | 27.33 ± 0.10 | 25.46 ± 0.01 | 24.68 ± 0.01 | UVES |
| 2025-09-14 | 2.14 | - | 25.43 ± 0.01 | - | UVES |
| 2025-09-20 | 1.97 | - | 25.61 ± 0.02 | - | X-shooter |
| 2025-09-22 | 1.92 | - | 25.70 ± 0.02 | 25.24 ± 0.05 | X-shooter |
| 2025-09-23 | 1.90 | - | 25.72 ± 0.02 | 25.32 ± 0.05 | X-shooter |
| 2025-09-24 | 1.87 | - | 25.73 ± 0.02 | 25.41 ± 0.05 | X-shooter |
| 2025-09-25 | 1.85 | - | 25.73 ± 0.02 | 25.39 ± 0.05 | X-shooter |

Notes. In Tables A.3 and A.4, the spectra obtained on September 3 and 4 in very similar circumstances were averaged to increase the signal-to-noise ratio. OH production rates were only measured in the UVES spectra. CN production rates before August 21, 2025 can be found in Rahatgaonkar et al. (2025).

Appendix B: Evolution of NiI and FeI emission lines

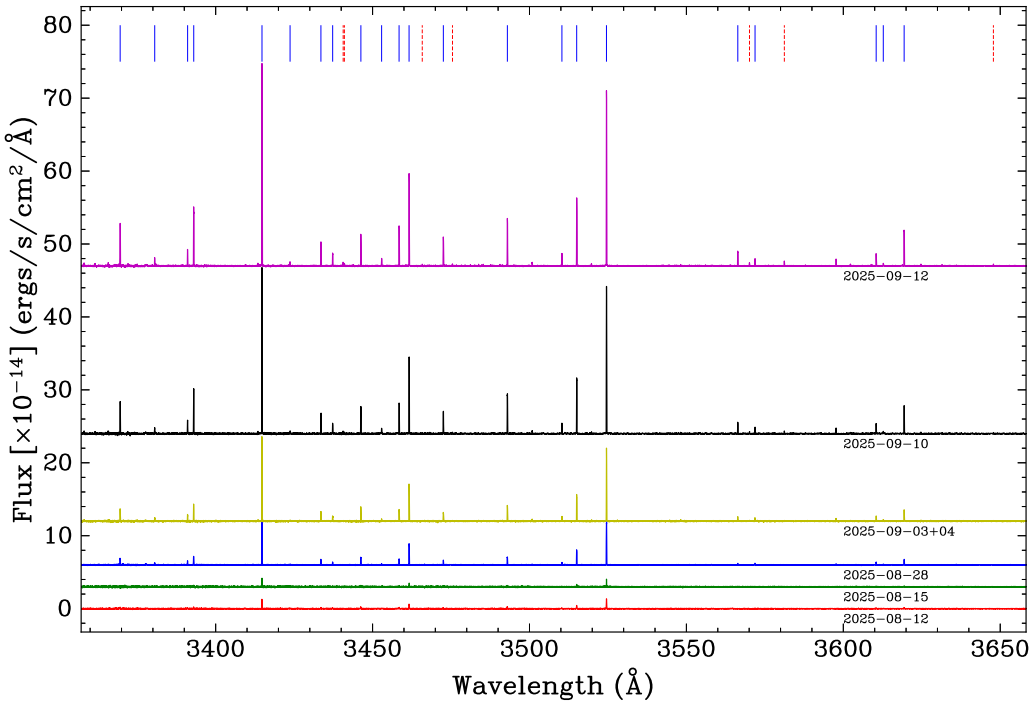


Fig. B.1. UVES blue, continuum-subtracted, spectra of comet 3I from August 12 to September 12. They show the evolution of the NiI (solid blue tickmarks) and FeI lines (dashed red tickmarks) in the spectral range 3360–3650 Å. The flux scale is identical for all spectra, which are shifted vertically for clarity.

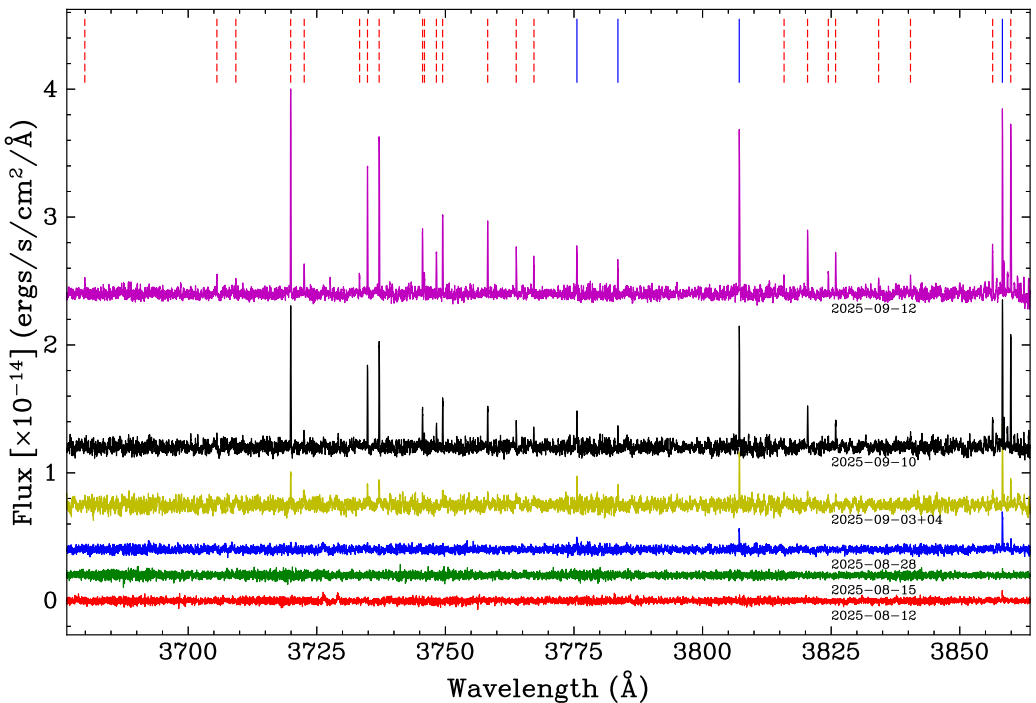


Fig. B.2. Same as Fig. B.1 for the 3680 - 3860 Å spectral range.